ISAS - INTERNATIONAL SCHOOL
FOR ADVANCED STUDIES

Scuola Internazionale Superiore di Studi Avanzati

International School for Advanced Studies

Coherent transport of electrons and holes in semiconductors in weak magnetic fields

Thesis submitted for the degree of

"Magister Philosophiæ"

CANDIDATE

Guido Goldoni

SUPERVISOR

Dott. Annalisa Fasolino

October 1991

TRIESTE

SISSA - SCUOLA
INTERNAZIONALE
SUPERIORE
STUDI AVANZATI
TRIESTE
Strada Costiera 11

Scuola Internazionale Superiore di Studi Avanzati

International School for Advanced Studies

Coherent transport of electrons and holes in semiconductors in weak magnetic fields

Thesis submitted for the degree of

"Magister Philosophiæ"

CANDIDATE

Guido Goldoni

SUPERVISOR

Dott. Annalisa Fasolino

October 1991

Acknowledgements

I would like to express my thanks to my supervisor Annalisa Fasolino, particularly for continuous encouragement. I also benefited from the help and friendship of many people in SISSA which I will indicate with the collective name of Pasquale Pavone.

Table of Contents

Introduction

In this thesis we investigate the coherence effects of ballistic *valence* electrons in semiconductor nanostructures. Recently coherent motion has been experimentally observed in *conduction* electrons in Transverse Electron Focusing (TEF) experiments realized in heterojunction devices [1]. In this work we make use of a simple model to calculate focusing spectra for a two-dimensional hole gas and interpret the results within the semiclassical approach.

Nanostructures are semiconductor systems where carriers are confined in one or more dimensions on a lengthscale comparable to their wavelength (reviews on the subject can be found in refs. [2, 3, 4]). Two-dimensional as well as one-dimensional (quantum wires) or zero-dimensional (quantum dots) systems can be realized by combining several techniques like molecular beam epitaxy, etching and lithography.

Due to the confinement, optical and transport properties of these structures are strongly affected by quantum effects. Since the confining potential depends on the dimensions and geometry of the device and can generally be tuned by means of applied fields, the possibility of having quantum devices of tunable characteristics arises. Tunable optical transitions, resonant tunnelling, quantized conductances, etc. make nanostructures of technological interest. On the other hand, they are a test of many simple quantum mechanical models.

New areas of research opened when high-mobility two-dimensional systems were realized in layered structures. In these structures, contrary to the bulk doped semiconductors,

carriers can be spatially separated from the ionized impurities, leading to the suppression of one of the most limiting scattering mechanisms at low temperatures. Among the new quantum effects, one of the most recent is the realization of the ballistic regime, *i.e.* carrier motion without incoherent scattering on the scale of the device dimensions. In the ballistic regime the coherence of the wavefunction is maintained during the carrier motion and interference effects may arise. This effect has been experimentally investigated by transverse electron focusing [1, 5, 6], a well-known technique based on the ballistic motion of electrons in the weak magnetic field regime. While in metals the electron focusing experiments can be explained making use of classical mechanics only, recent experiments performed in the two-dimensional electron gas in heterostructures[1] cannot be completely understood in a purely classical scheme, confirming that electronic motion in semiconductors is dominated by coherence effects [7]. The coherent nature of the motion has also been demonstrated in semiconductor one-dimensional wires [8].

At the same time the interest increases in theoretical models to describe the electronic structure of such systems [2]. It is now a well-known fact that valence and conduction states in confined systems behave very differently. Valence states are the result of the binding between the p states of the bulk host material. Their degeneracy at the Γ point complicates the problem of the calculation of the electronic structure in confined systems, where strong non-parabolicities of the valence band and warping of the Fermi surface appear. In this work we introduce a model effective hamiltonian which is intended to simulate the in-plane dispersion of the topmost valence subbands of a GaAs–$Al_xGa_{1-x}As$ quantum well near the Γ point. Then we use the model in a semiclassical formulation of the focusing problem [7, 10] to calculate how the focusing phenomena would modify if a hole gas is used instead of a conduction electron gas.

We find that warping of the Fermi surface may result in an enhancement of the focusing in some crystallographic directions. Moreover we show that focusing experiments with holes may probe directly the valence band structure [9].

In chapter 1 we review the experimental results concerning electron focusing both in metal and semiconductors and in chapter 2 we state the semiclassical formulation of the focusing phenomena in semiconductors. In chapter 3 we summarize the multiband effective mass approximation and we introduce a model hamiltonian for the valence subbands of a quantum well. Finally, in chapter 4 we use this hamiltonian to calculate the focusing spectrum of a two-dimensional hole gas and we compare the results with the focusing spectra calculated for a two-dimensional electron gas.

Chapter 1

Transverse electron focusing experiments

In this chapter the basic ideas and experimental evidences of transverse electron focusing both in metals and in semiconductors are presented. Also some characteristics of the two-dimensional electron gas in semiconductors are described. The different nature of the electron focusing phenomenon in metals and semiconductors is emphasized.

1.1 The transverse electron focusing technique: the case of metals

It has been shown by Sharvin [5, 11, 12] and Tsoi [6, 13] that a magnetic field can focus ballistic electrons in *metals*. A typical arrangement, similar to that used by Sharvin and Tsoi, is schematized in fig. 1.1. A magnetic field B is applied onto a single-crystal metallic sample where two small contacts I and C are realized a distance L far apart. The distance L between the contacts is such that

$$\boxed{L < l_e}$$

where l_e is the elastic mean free path which, in metals at low temperature, can be of the order of several millimeters; this regime is called *ballistic*. Electrons moving with the

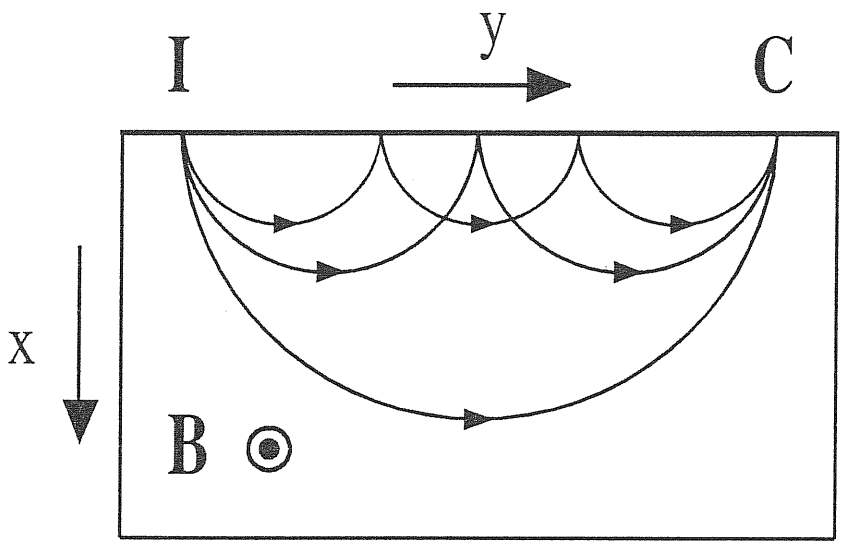

Figure 1.1: Geometry of a transverse electron focusing experiment. Electrons move from I to C under the influence of the magnetic field. Skipping orbits up to two reflections are shown. The magnetic field is normal to the plane of the orbits.

Fermi velocity are injected at I. The motion of ballistic electrons in metals can be thought of as that of free electrons: from the classical equations of motion

$$m\ddot{\mathbf{r}} = -\frac{e}{c}(\mathbf{v} \times \mathbf{B}) \tag{1.1}$$

where m and e are the mass and charge of the particle and v is its velocity, one obtains that a charge in a magnetic field moves in circular orbits (*cyclotron orbits*) in a plane normal to the field with radius

$$r_{cycl} = \frac{mvc}{eB} \tag{1.2}$$

and frequency

$$\omega_c = \frac{v}{r_{cycl}} = \frac{eB}{cm}. \tag{1.3}$$

For an electron with the Fermi velocity $v_F = \hbar k_F/m$, one obtains

$$r_{cycl} = \frac{c\hbar k_F}{eB} \tag{1.4}$$

where k_F is the Fermi wave vector.

Transverse electron focusing (TEF) experiments consist in measuring the voltage drop at the collector C as a function of the magnetic field while keeping fixed the injected current. From the classical description above, a peak in the collector voltage is expected when B is such that $L = 2r_{cycl}$. Using eq. (1.4),

$$B_{focus} = \frac{2c\hbar k_F}{eL} \tag{1.5}$$

which is called *focusing field.* Since during the path between I and C electrons may have

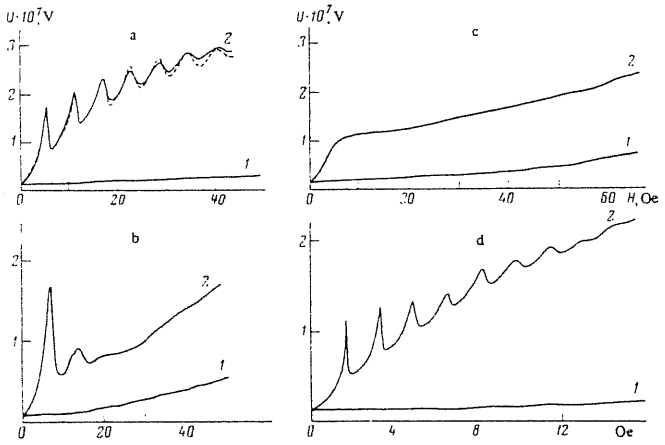

Figure 1.2: TEF spectra in metals under different conditions[13]. Spectra (a) and (d) show a high number of well-defined sharp peaks at the classical focusing fields due to specular reflections on the boundary. Spectra (b) and (c) where taken after introducing different kinds of damage in the sample.

gone through one or more reflections upon the boundary of the sample (*skipping orbits*), higher order peaks are expected at fields such that L is an integer multiple of $2r_{cycl}$, *i.e.* at $B = iB_{focus}, (i = 1, 2, \ldots)$, the i-th peak being caused by the orbit with $i - 1$ reflections. Some of the orbits satisfying this condition are shown in fig. 1.1. The point contacts behave as classical probes since their width ($\sim 1\mu m$) is large compared to the Fermi wavelength λ_F in metals, typically of the order of $0.5nm$. The measured TEF spectra reported in fig. 1.2 confirm this classical picture showing a series of equidistant well defined peaks at

multiples of B_{focus}. Since the scattering against the boundary is only partially specular, higher order peaks decrease in amplitude due to the higher number of reflections.

Due to the simple interpretation of the spectra, TEF in metals has become a well established technique to obtain a number of informations on the shape of the Fermi surface [11], on the surfaces of metals [13, 14] and on the electron-phonon interaction [15].

1.2 The two-dimensional electron gas in semiconductors

TEF measurements concern transport of electrons in the plane normal to the magnetic field. This makes possible to obtain TEF spectra also in semiconductors since high mobility (and consequently ballistic regime) is achievable in the two-dimensional electron gas (2DEG) confined *e.g.* at the GaAs–$Al_xGa_{1-x}As$ heterojunction. The enhanced mobility with respect to bulk semiconductors arises because in this kind of structures the carriers can be spatially separated from the donors as we will see below.

A typical semiconductor structure of this kind is depicted in fig. 1.3(a). On a GaAs substrate a layer of undoped $Al_xGa_{1-x}As$ is grown with a typical value of $x = 0.35$ and a thickness of the order of $100nm$. On top of this, a layer of n-type doped AlGaAs is grown. Since the bottom of the AlGaAs conduction band lies higher in energy than that of GaAs, electrons from the donor states in the doped layer move to the GaAs substrate. As a consequence of the Fermi level line-up, electrons remain confined in a well in the growth direction, approximately triangular in shape, at the GaAs–$Al_xGa_{1-x}As$ interface, as shown in fig. 1.3(b), while they are free to move in a plane parallel to the interface. As a result electrons in the 2DEG move in (undoped) GaAs while impurity ions are confined in the doped AlGaAs layer. This allows one to obtain an high mobility electron gas. The thickness of the undoped AlGaAs layer is chosen large enough that the (long range) Coulomb potential generated by the impurity ions is small in the 2DEG, but not so large as to inhibit the charge transfer from the doped layer to the undoped 2DEG.

In order to realize the point contacts for the TEF arrangement, narrow constrictions

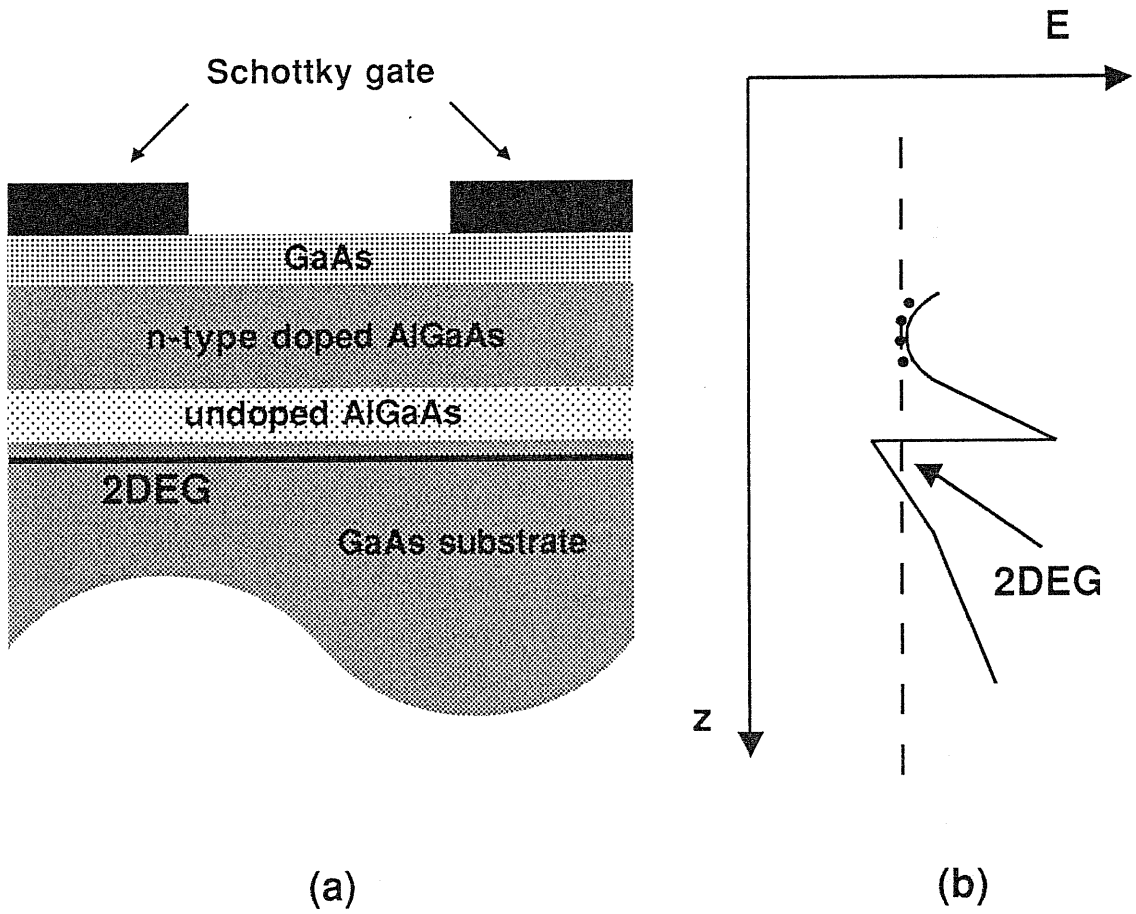

Figure 1.3: a) GaAs–$Al_xGa_{1-x}As$ heterojunction device with a split Schottky gate. b) Profile of the bottom of the conduction band in the growth direction after charge transfer from n-type AlGaAs to GaAs. The dashed line represent the chemical potential. Dots represent impurity states in the doped layer.

can be obtained in the 2DEG by means of split Schottky gates, an example of which is shown in fig. 1.3(a) on top of the heterojunction. These consist of metal depositions whose depletion regions extend under the gate into the 2DEG. With a suitable geometry, quasi one-dimensional channels can be realized in the 2DEG which can serve to inject electrons in the wide two-dimensional region.

1.3 TEF in semiconductors: coherence effects

The device

The first evidence of electron focusing in semiconductors has been obtained by van Houten *et al.* [1] in 1988. They obtained a 2DEG at the GaAs–$Al_xGa_{1-x}As$ interface with $l_e \approx 9\mu m$ with the distance between the contacts in the range $1.5\mu m \div 3\mu m$ so that ballistic regime was achieved. Two point contacts were defined with split Schottky gates on top of the

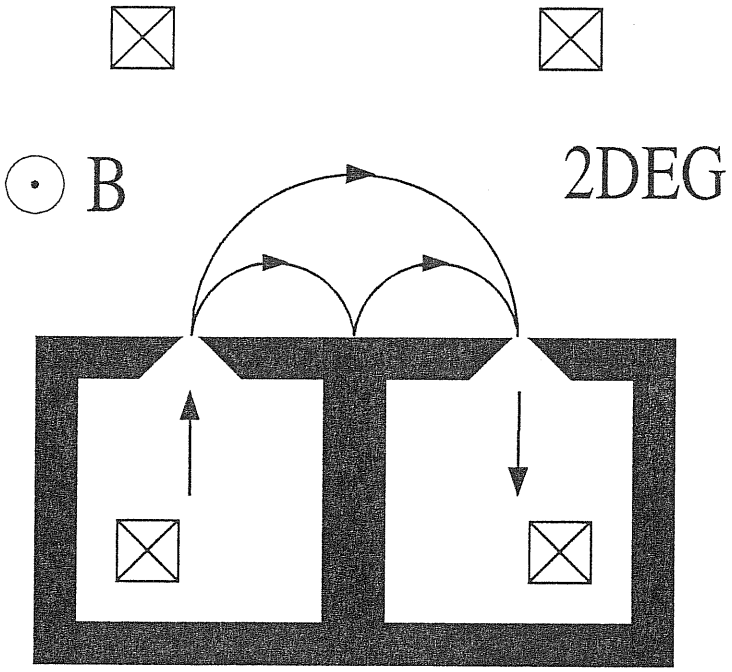

Figure 1.4: Double point contacts geometry for the TEF experiments in semiconductors. The black area represents the Schottky gate defined in the xy plane on top of the device. The field is along z. The four crossed squares represent Ohmic contacts.

heterojunction device, with the geometry shown in black in fig. 1.4. The contacts are essentially electron *reservoir* separated from the bulk 2DEG. Note that the width W of the contacts can be tuned via the gate voltage and can vary from $250nm$ down to pinch-off.

The small width of the contacts is responsible for quantized conductivity [16] due to the lateral confinement; this giustifies the name of *quantum point contacts.*

Coherent focusing

The focusing phenomenon in this device differs in an important way from electron focusing in metals: the width of the point contacts is comparable with the high λ_F of the 2DEG (typically $40nm$); since the distance L between the contacts is smaller then the phase coherence length, they become sensitive to interference effects. This *quantum regime* manifests itself in the spectra reported by van Houten *et al.* [1] shown in fig.1.5. At low fields a series of equidistant well-defined peaks is present at the classical focusing fields, resembling the case of metals. Nevertheless, new features appear; a strong fine structure is superimposed to the peaks. This fine structure is reproducible in the same sample if the gate potential is unchanged. The intensity of the fine structure increases with the magnetic field and at high fields ($\geq 0.4T$) the resemblance to the classical focusing spectra is lost. The fine structure is smeared out if the temperature or the width of the point contacts are increased. Note that the high number of classical focusing peaks observed at low fields demonstrates that scattering of electrons against the barrier is chiefly specular.

As we shall see in chapter 2, a theoretical investigation by Beenakker *et al.* [7] has shown that the presence of the fine structure is the result of the interference between the quantum states of the problem; for this reason electron focusing in semiconductors has been called *coherent focusing.*

Relationship with the Hall regime

In the device of fig. 1.4 four Ohmic contacts are shown. The actual quantity measured in a TEF experiment is the voltage drop between the collector and one of the contacts divided by the injected current. In this geometry both longitudinal and Hall resistance can be measured, depending on how the Ohmic contacts are connected. The spectra shown in fig. 1.5 are taken in the Hall configuration. For this reason the focusing peaks due to ballistic electrons are superimposed to a linearly growing Hall resistance due to diffusively

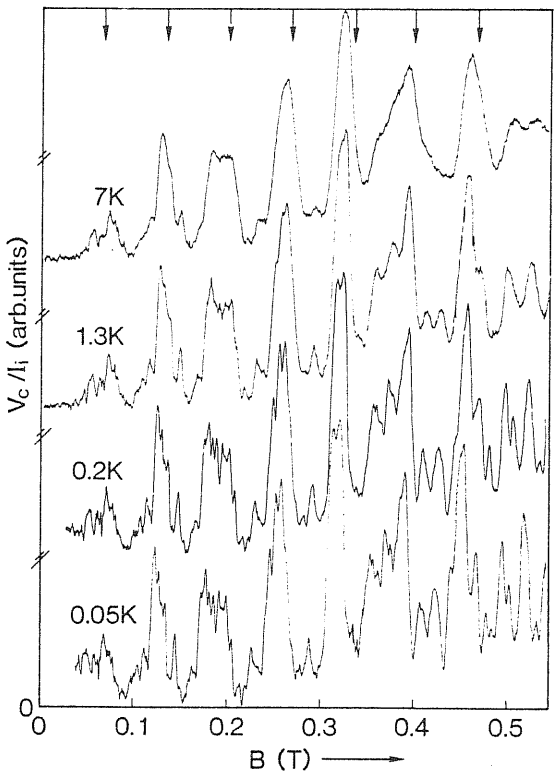

Figure 1.5: TEF spectra in semiconductor heterostructures at different temperatures from ref. [10]. The vertical arrows indicate the classical focusing fields.

moving background electrons; the focusing spectrum is alternatively higher and lower of the background Hall resistance. The Hall resistance can be singled out if the direction of the field is reversed since electrons do not move anymore towards the collector and they all contribute to the background. At higher fields ($> 1T$), when the cyclotron diameter is smaller then the width of the contacts, the resolution for the focusing is insufficient and the linear Hall resistance is displayed. At sufficiently high fields the characteristic platous of the quantum Hall effects appear.

Note that TEF experiments correspond to the measure of a *non-local* resistance both from a classical and quantum point of view since the distance between the probes is lower than the mean free path and *a fortiori* lower then the phase coherence length. The

manifestation of the non-locality is the presence of the focusing peaks *and* of the fine structure.

So far TEF experiments have been performed in a 2DEG, *i.e.* in a n-type doped semiconductor. The problem we address in this work is how TEF spectra would be modified in a two-dimensional *hole* gas, which in principle could be obtained in a p-type doped heterojunction device.

Chapter 2

The semiclassical description of electron focusing

Since the classical picture is insufficient to describe electron focusing in semiconductors, we look for a quantum description of the phenomena. In this chapter we perform a theoretical analysis of TEF experiments from this point of view, we explain what the edge magnetic states are and their relevance to the TEF experiments and how the collected current can be calculated in a semiclassical approximation.

2.1 Edge magnetic states for conduction electrons

We are interested in determining the relevant quantum states for electron focusing, *i.e.* the states of a free electron in a magnetic field near an infinite boundary. Let us first determine the states of a free electron in a magnetic field in bulk [17]. The appropriate hamiltonian can be obtained from the free electron hamiltonian by the substitution

Peierls substitution $$\mathbf{k} \rightarrow \mathbf{p} + \tfrac{e}{c}\mathbf{A} \tag{2.1}$$

of the canonical momentum operator $\mathbf{p}$, where $e = |e|$ is the electron charge, c is the velocity of light and $\mathbf{A}$ the vector potential. For a uniform field $\mathbf{B}$ along the z direction,

the Landau gauge

$$\mathbf{A} = (0, Bx, 0) \tag{2.2}$$

with $B = |\mathbf{B}|$ is appropriate to the geometry of our problem. From (2.1) and (2.2) the hamiltonian becomes

$$H = \frac{p_x^2}{2m} + \frac{p_z^2}{2m} + \frac{1}{2m}\left(p_y + \frac{e}{c}Bx\right)^2. \tag{2.3}$$

Here and in the following the Zeeman term will be considered negligible (Zeeman splitting is $\sim 10^{-1} meV$ at $B = 1T$). Since the operators y and z do not appear in H, plane waves are eigenfunctions of H in these directions. Writing the wavefunction ψ as

$$\psi(x, y, z) = e^{ik_y y} e^{ik_z z} \chi(x) \tag{2.4}$$

one can decompose the motion along z, which remains a free motion, from that in the plane perpendicular to the field and obtain the Schrödinger equation of an harmonic oscillator with frequency $\omega_c = eB/mc$ in the x direction, centered around $x_0 = -c\hbar k_y/eB$:

$$\left[\frac{p_x^2}{2m} + \frac{m\omega_c^2}{2}(x - x_0)^2\right] \chi(x) = (E - \frac{p_z^2}{2m})\chi(x) \tag{2.5}$$

Then the eigenvalues E are

$$E = \hbar\omega_c(n + \tfrac{1}{2}) + \frac{p_z^2}{2m} \qquad n = 0, 1, 2, \ldots \tag{2.6}$$

Then one finds that the magnetic field splits the parabolic energy spectrum of the motion in the xy plane into the quantized Landau levels. We have seen in the previous chapter that in semiconductor heterostructures it is also possible to quantize the motion along z, thus realizing a two-dimensional electron gas. In chapter 3 we will calculate the consequences of such confinement on the electronic structure.

Note that x_0, which corresponds to the centre of the classical orbit in the x direction, depends on the momentum in the y direction and is a good quantum number in this gauge since it commutes with the hamiltonian of eq. (2.5). Defining the *magnetic length* as

$$l_m = \left(\frac{c\hbar}{eB}\right)^{1/2} \tag{2.7}$$

the adimensional quantities $\overline{x}_0 = x_0/l_m$ and $\overline{k}_y = k_y l_m$ satisfy the identity $\overline{x}_0 = -\overline{k}_y$. The situation is described in fig. 2.1(a). Each state is labelled by the quantum numbers n, x_0, but, since the energies ε are independent from x_0, each level has a degeneracy equal to the number of allowed values of x_0. Consider a box in the xy plane of sides L_x and L_y, much larger then the cyclotron radius, and impose periodic boundary conditions. Then k_y assume discrete values with density $(L_y/2\pi)$. x_0 must assume values in $(0, L_x)$ so that from the definition of x_0 we have $\Delta k_y = eBL_x/c\hbar$. Then the total degeneracy is

$$\nu = (L_y/2\pi)\Delta k_y = \frac{L_x L_y}{2\pi}\frac{eB}{\hbar c}. \tag{2.8}$$

The separation between the levels and their degeneracy increases with increasing field, giving rise to oscillations in the Fermi energy at high fields, when only few Landau levels are populated, which in turn are responsible for many oscillatory behaviours in transport properties.

Now let us put a boundary $V(x)$ along the x direction (see fig. 1.1 for the choice of the axis). Then x_0 remains a good quantum number but the degeneracy is broken. While for x_0 far from the boundary the situation is similar to the free electron case, in proximity of the boundary the condition of the vanishing of the wavefunction modifies the energy levels. In the simple case of x_0 coinciding with the boundary it is easily seen that the allowed states are those Landau levels which correspond to odd n (see fig. 2.1(b)). For arbitrary x_0 energies vary continuously. The important point is that a confining potential splits the degeneracy and allowed states labelled by x_0 arise between the bulk Landau levels. These are called *magnetic edge states* and are the quantum analog of the skipping orbits defined in chapter 1. Complete quantum mechanical calculations of the edge energies are available in literature [18]. Nevertheless, since at low fields electrons are localized over a distance much larger then the period of the crystalline potential, we are in the limit where the semiclassical approximation applies. This has the advantage of reducing the calculation of the edge states to a geometric problem which is suitable to be used with different shapes

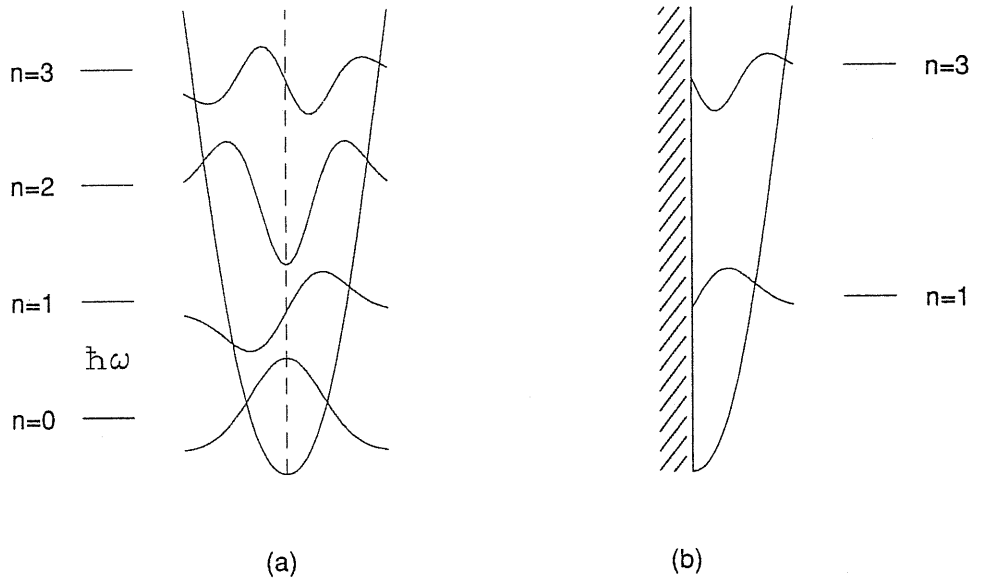

Figure 2.1: a) Free electron in a uniform magnetic field. Its energies and wavefunctions are those of the harmonic oscillator. b) Electron in a magnetic field with x_0 on the boundary (shaded area). Only states with odd n are allowed. For arbitrary x_0 energies lie in between; then the presence of a boundary splits the Landau levels degeneracy.

of the Fermi surface.

In the semiclassical model one considers electrons in a given periodic potential and a given dispersion curve $\varepsilon(\mathbf{k})$. Then, with no electric field, the vector $\mathbf{k}$ satisfies the semiclassical equations of motion

$$\mathbf{v}_n(\mathbf{k}) = \frac{1}{\hbar}\frac{\partial \varepsilon_n(\mathbf{k})}{\partial \mathbf{k}}, \tag{2.9}$$

$$\hbar\dot{\mathbf{k}}(t) = -\left[\frac{e}{c}\mathbf{v}_n(\mathbf{k}) \times \mathbf{B}(\mathbf{r},t)\right], \tag{2.10}$$

where n is the band index. Since $\mathbf{k}$ does not change in the direction of $\mathbf{B}$, the energy and the component of $\mathbf{k}$ parallel to B are both constant of motion; electrons move in k space on a curve which is the intersection of the equal energy surface with a plane normal to the field. Multiplying (2.10) from the left by a unit vector in the direction of the field $\hat{\mathbf{B}}$

we obtain

$$\hat{\mathbf{B}} \times \hbar\dot{\mathbf{k}}(t) = -\frac{eB}{c}\hat{\mathbf{B}} \times (\dot{\mathbf{r}} \times \hat{\mathbf{B}}) = -\frac{eB}{c}\left(\dot{\mathbf{r}} - \hat{\mathbf{B}}(\hat{\mathbf{B}} \cdot \dot{\mathbf{r}})\right) = -\frac{eB}{c}\dot{\mathbf{r}}_\perp \tag{2.11}$$

where $\mathbf{r}_\perp$ is the projection of the orbit in the plane normal to the field. Integrating the last equation we get

$$\mathbf{r}_\perp(t) = -\frac{\hbar c}{eB}\hat{\mathbf{B}} \times \mathbf{k}(t). \tag{2.12}$$

Then the projection of the real space orbits $\mathbf{r}(t)$ are obtained rotating $\mathbf{k}(t)$ of $\pi/2$ around the direction of the field and multiplying by l_m^2. One the same basis, it is possible to write the Bohr–Sommerfeld quantization condition

$$\frac{1}{\hbar}\oint \mathbf{p} \cdot d\mathbf{q} = 2\pi(n - \gamma), \tag{2.13}$$

where $\mathbf{q}$ and $\mathbf{p}$ are conjugate variables and γ is a constant to be determined later, in a real space condition [19]; in fact, from (2.1) and (2.12),

$$\oint \mathbf{p} \cdot d\mathbf{q} = \oint \left(\hbar\mathbf{k} - \frac{e}{c}\mathbf{A}\right) \cdot d\mathbf{r} = \frac{e}{c}\oint [(-\mathbf{r} \times \mathbf{B}) - \mathbf{A}]\, d\mathbf{r}.$$

Using standard vector analysis identities one can prove that

$$\oint(\mathbf{r} \times \mathbf{B}) \cdot d\mathbf{r} = -\oint \mathbf{B} \cdot \mathbf{r} \times d\mathbf{r} = -2\int_S \mathbf{B} \cdot d\boldsymbol{\sigma},$$

$$\oint \mathbf{A} \cdot d\mathbf{r} = \int_S \nabla \times \mathbf{A} \cdot d\boldsymbol{\sigma} = \int_S \mathbf{B} \cdot d\boldsymbol{\sigma},$$

where S is the surface enclosed by the trajectory in real space. Then eq. (2.13) becomes

$$\frac{e}{\hbar c}\int_S \mathbf{B} \cdot d\boldsymbol{\sigma} = 2\pi(n - \gamma). \tag{2.14}$$

The simple interpretation is that the flux of the magnetic field enclosed by the trajectory is quantized in multiples of $\frac{hc}{e}$. Eq. (2.14) is completely general provided the right value of γ is chosen, depending on the boundary conditions. γ accounts for abrupt variations of the phase of the wavefunction in correspondence of particular surfaces. One of these surfaces is an infinite boundary, which causes the wavefunction to change its phase of π

since incident and reflected waves must cancel each other. One other surface is a caustic, *i.e.* the *loci* of points where the density of classical trajectories becomes infinite. It can be shown [20, 21] that passing trough these points makes the wavefunction change its sign, bringing a change of $\pi/2$ in the phase. In the case of a skipping orbit the flux to be quantized is that between the orbit and the boundary. The one-dimensional periodic motion along x is comprised between the boundary and a caustic so that the right value of γ is $1/4$. Note that the motion of a free electron in a magnetic field is comprised between two caustics and the appropriate value of γ is $1/2$ which gives the right value for the zero point energy of the harmonic oscillator problem.

Conduction electrons in the 2DEG near the band edge have a parabolic energy dispersion $\varepsilon = \hbar^2 k^2/2m$ so that the Fermi energy surfaces in two dimensions are circles. Then the real space orbits are circles as well and the integral in (2.14) is done by calculating the area between the circular orbit and the boundary. The radius of the orbit r_{cycl} depends on the energy:

$$r_{cycl} = l_m^2 k = l_m^2 \frac{\sqrt{2m\varepsilon}}{\hbar}. \tag{2.15}$$

Then eq. (2.14) is a condition on the allowed energies. One can show by simple geometry that eq. (2.14) becomes

$$2\frac{\varepsilon}{\hbar\omega_c}\left\{\arccos\zeta - \zeta(1-\zeta^2)^{1/2}\right\} = 2\pi(n-\gamma), \tag{2.16}$$

where $\zeta = -k_y/\sqrt{2m\varepsilon}$. Eq. (2.16) is an implicit equation in the energy whose solutions are found numerically and shown in fig. 2.2 as a function of k_y, which is equivalent to the centre of the trajectory. At fixed energy only a finite number of values of k_y satisfy eq. (2.16). For positive k_y the centre of the orbit is *inside* the barrier and energies increase because the electron is bound near the barrier by the field. For negative k_y, the centre of the orbit moves away from the boundary and energies tend to the bulk Landau levels (dashed lines) even if the two solutions do not connect continuously due to the change in γ, since the semiclassical approximation do not take into account the extension of the

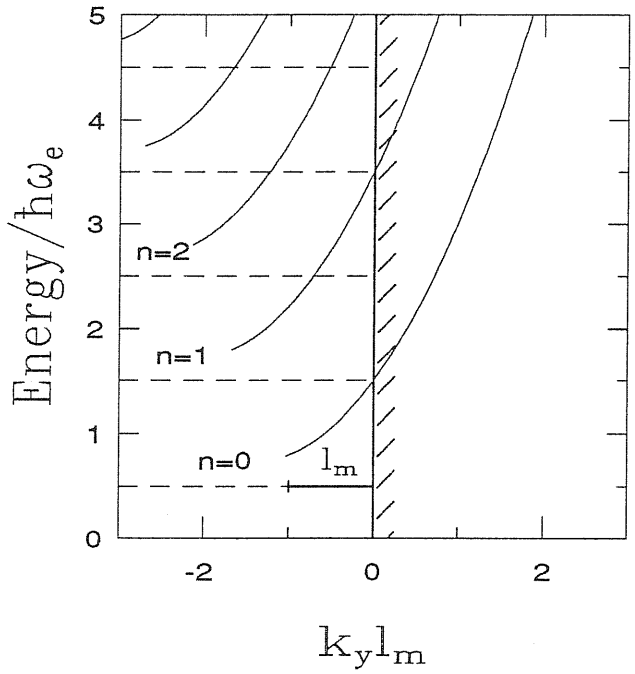

Figure 2.2: Edge magnetic state energies for conduction electrons (solid lines). The central shaded area represent the boundary. Dashed lines represent bulk Landau levels.

wavefunction outside the orbit. Note that for $k_y = 0$ we obtain the states corresponding to fig. 2.1(b). The states relevant to the transport are the magnetic states only, having a non-vanishing $\frac{\partial \varepsilon}{\partial k_y}$.

2.2 Calculation of the current

In the previous paragraph we stated that an electron moving in a TEF arrangement propagates through the edge states at the Fermi energy corresponding to discrete values of k_y. Since we showed how the magnetic edge states can be calculated for an arbitrary shape of the Fermi surface from eq. (2.14), we need a method to calculate the current from the k_n's.

The number n_{max} of involved propagating modes is equal to the number of occupied Landau levels, as it can be guessed from fig. 2.2. Since the distance travelled by the

electrons is much smaller than the phase coherence length, the current at the collector is the result of the interference between the coherently excited n_{max} modes. This becomes clear by calculating the wavefunction at the field B in the WKB approximation [21], as the sum over the classical trajectories (all the skipping orbits which end up at the collector) of a phase factor $e^{i\phi}$, where ϕ is the sum of $\frac{1}{\hbar}\int \mathbf{p}\cdot d\mathbf{l}$ with $\mathbf{l}$ running over the trajectory from the injector to the collector, plus a constant term due to reflections and passages through the caustics. The calculations where carried out explicitly by Beenakkers and coworkers [7, 10] for conduction electrons. They also showed that this real space formulation of the wavefunction can be translated in a reciprocal space expression by the method of the stationary phase applied to the sum over the trajectories, thus making explicit the relation between the wavefunction and the k_n's. The wavefunction can be finally connected to the current, since, due to the vanishing of the wavefunction at the boundary, we have

$$I_c \propto \left|\frac{\partial\psi(0,L)}{\partial x}\right|^2 \tag{2.17}$$

where $\psi(0,L)$ is the wavefunction calculated at the collector. The final result is

$$I_c \propto \frac{1}{l_{cycl}^2}\left|\sum_{n=1}^{n_{max}} e^{ik_nL}\right|^2 \tag{2.18}$$

where k_n are the n_{max} momenta k_y at the Fermi energy, *i .e.* the k_y values corresponding to the intercepts between E_F and the magnetic edge states. Equation (2.18) shows that electrons move from the injector to the collector as plane waves with momentum determined by the magnetic field and that constructive or destructive interference can occur at L.

Spectra calculated from eq. (2.18) for conduction electrons will be discussed in chapter 4 and compared with focusing spectra obtained for valence electrons.

Chapter 3

Electronic structure of two-dimensional systems

As we have seen in chapter 2, a z-directed magnetic field quantizes the motion in the xy plane. In this chapter we review the basic features of the electronic structure in a two-dimensional system, *i.e.* a system where a confining potential quantizes also the motion along z. In particular we analyze the behaviour of the valence band in the framework of the multiband effective mass approximation. Then a simple model hamiltonian is presented which is intended to simulate a realistic in-plane dispersion of the valence band in a GaAs–$Al_xGa_{1-x}As$ heterostructure near the Γ point.

3.1 Two-dimensional confinement: an ideal model

We have sketched in §1.2 how in a heterostructure the electron gas is confined in a layer. From a quantum mechanical point of view, electronic states in a heterostructure are the result of a confining potential well of asymmetric shape in the growth direction. Moreover a realistic calculation should take into account the charge redistribution self-consistently. In what follows we will neglect band bending (*flat band approximation*) and consider how bulk band structure modifies in a symmetric quantum well. At the end of the chapter we

will discuss the effects of the asymmetry of the confining potential.

In the simplest approximation electrons in a heterostructure are free to move in a plane normal to the growth direction (taken to be the z axis) so that the wavefunction can be factorized as $\psi(x,y,z) = e^{ik_x x}e^{ik_y y}\chi(z)$ and the Schrödinger equation reads

$$\left[-\frac{\hbar^2}{2m^*}\frac{d^2}{dz^2} + V(z)\right]\chi(z) = (\varepsilon - \frac{\hbar^2 k_x^2}{2m^*} - \frac{\hbar^2 k_y^2}{2m^*})\chi(z) \tag{3.1}$$

where $V(z)$ is the square well potential, k_x and k_y are the in-plane wavevectors and m^* is the effective mass of the bulk material. The bound solutions of this problem are well known and consist of discrete levels ε_n which, in the limit of an infinite well, are given by

$$\frac{\hbar^2\pi^2}{2m^*L^2}n^2 \tag{3.2}$$

with respect to the bottom of the well, where L is the width of the well and n is an integer ≥ 1 (see top of fig. 3.1). Therefore the full energy spectrum consists of a series of parabola in k_x, k_y starting from each of the ε_n edges:

$$\varepsilon_{nk_xk_y} = \varepsilon_n + \frac{\hbar^2 k_x^2}{2m^*} + \frac{\hbar^2 k_y^2}{2m^*}. \tag{3.3}$$

It can be shown that a bound state is always present in one-dimensional wells, no matter how shallow the well is. Motion in the z direction is prohibited as far as transitions between the levels are not allowed, *i.e.* if the level spacing is larger than the thermal or collisional broadening. To give an order of magnitude, for the GaAs conduction band $(m^*/m_0 = 0.067)$ with $L = 100\mathring{A}$, we have $\frac{\hbar^2\pi^2}{2m^*L^2} \sim 56meV$.

For completeness we note that the two-dimensional density of states differs in a qualitative way from the three-dimensional one. The density of state is defined by

$$\rho(\varepsilon) = \sum_{k_xk_yn} \delta(\varepsilon - \varepsilon_{nk_xk_y}) \tag{3.4}$$

with $\varepsilon_{nk_xk_y}$ given by (3.3). By imposing cyclic boundary conditions in a box of sides L_x and L_y, one can substitute $\sum_{k_xk_y} \rightarrow \frac{L_xL_y}{(2\pi)^2}\int dk_x dk_y$. By further substituting $\zeta = k^2$ the

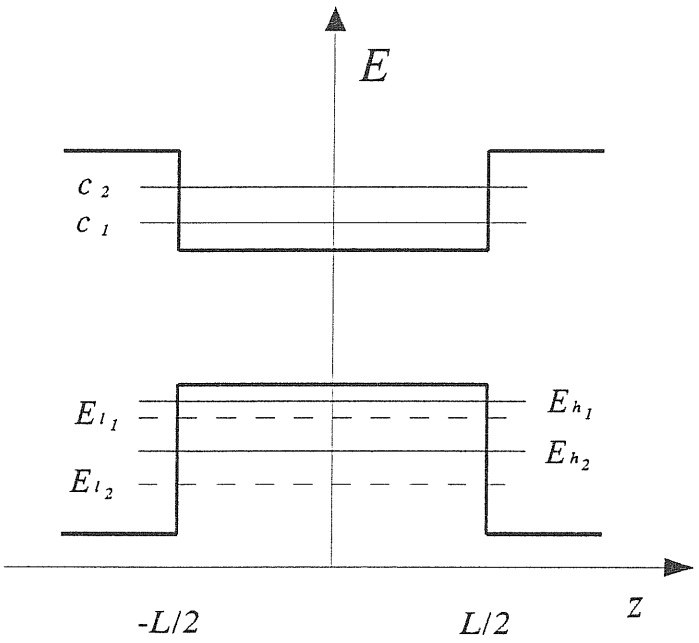

Figure 3.1: Splitting of the conduction edge (top) and of the heavy and light holes (bottom) in a quantum well. Solid horizontal lines represent the first two heavy hole subband edges. Dashed lines represent the light hole subbands.

integral gives

$$\rho(\varepsilon) = 2\frac{m^* L_x L_y}{2\pi\hbar^2} \sum_n \theta(\varepsilon - \varepsilon_n) \tag{3.5}$$

where $\theta(x)$ is the step function. The two-dimensional density of state therefore is constant starting from ε_1 (and not from 0 due to the confinement) and increases stepwise each time the energy passes a new edge.

3.2 One step further: the multiband effective mass approximation

The situation for the valence band is much more complicated. The bulk band structure around the direct energy gap is sketched in fig. 3.2 along the k_z direction. For the most common semiconductors, it can be shown that the bulk valence states at the Γ point arise, from a tight-binding point of view, from the bonding p states. These are six states

(including spin) which are found to be split by the spin-orbit coupling in a four-fold degenerate state (labelled J=3/2) and a two-fold degenerate state (labelled J=1/2) at Γ, the splitting being Δ_{so} in fig. 3.2. The degeneracy complicates the problem in the sense that a single band picture, like that of the previous paragraph, breaks down. In the following we will see how the problem can be approached in the framework of the $\mathbf{k} \cdot \mathbf{p}$ scheme [22], a method which is useful to describe electronic bands in proximity of special points of the Brillouin zone. This method allows to consider only Fourier components of the wavefunction whose wavelengths are comparable to the dimensions of the confining potential, with the crystalline potential (*i.e.* short wavelength variations of the potential) only entering the problem as a renormalization of the masses.

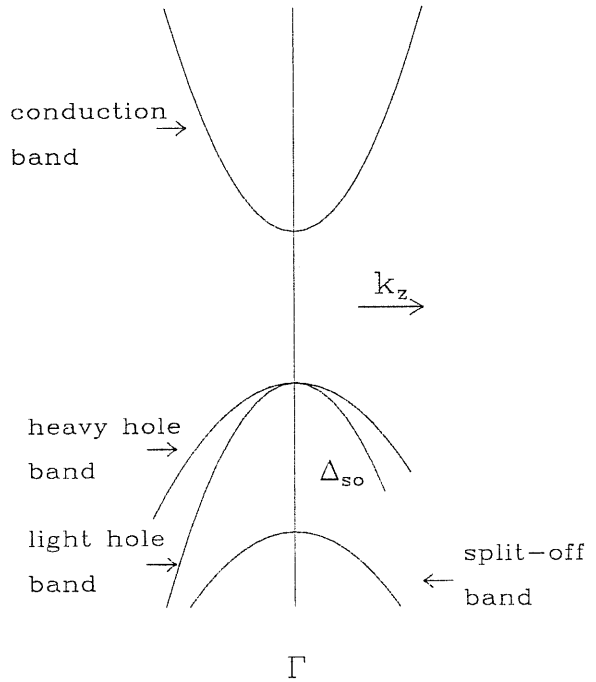

Figure 3.2: A typical band structure around the Γ point in a semiconductor in the k_z direction. The splitting Δ_{so} is due to spin-orbit coupling and is of the order of $.3eV$.

Our approach starts by writing the wavefunction at $\mathbf{k}$ making use of the Bloch states of the crystal at $\mathbf{k} = 0$, which are supposed to be the known eigenfunctions of the crystal

hamiltonian H. The basis is set up from the functions

$$|\nu\mathbf{k}>=\frac{e^{i\mathbf{k}\cdot\mathbf{r}}}{\sqrt{\Omega}}u_{\nu 0}(\mathbf{r}), \tag{3.6}$$

where $u_{\nu 0}$ is the periodic part of the Bloch states at $\mathbf{k}=0$ corresponding to the ν-th band. If one is interested, say, in the X point, the corresponding $u_{\nu X}$ functions should be used. Note that the $|\nu\mathbf{k}>$'s are not eigenfunctions of H. The $u_{\nu 0}$'s are orthogonal and normalized so that

$$\int u^*_{\nu 0}(\mathbf{r})u_{\nu' 0}(\mathbf{r})d\mathbf{r}=\delta_{\nu\nu'}. \tag{3.7}$$

The method is not exact anymore when the basis set is restricted to a finite number of bands; therefore it gives reasonable results only near the Γ point in contrast to tight-binding hamiltonians which give valid results all over the Brillouin zone. Nevertheless such complete knowledge of the band structure is seldom useful since properties of semiconductors heterostructures depends on electronic states lying few fractions of an electronvolt from the conduction and valence edges. Since quantum wells have typical dimensions of the order of 100Å, we are interested in states around Γ with $k\sim\pi/100\mathring{A}$. Thus a local knowledge is sufficient and may lead to computationally simple schemes.

To accomplish our program, we write the Schrödinger equation

$$(H+U)\,\psi_0(\mathbf{r})=\varepsilon\psi_0(\mathbf{r}), \tag{3.8}$$

where U is an external perturbing potential (*e.g.* the quantum well confining potential) and expand the wavefunction in the basis (3.6):

$$\psi_0(\mathbf{r})=\sum_{\nu\mathbf{k}}\phi_{\nu\mathbf{k}}|\nu\mathbf{k}>. \tag{3.9}$$

Then (3.8) becomes

$$\sum_{\nu'\mathbf{k}'}<\nu\mathbf{k}|H+U|\nu'\mathbf{k}'>\phi_{\nu'\mathbf{k}'}=\varepsilon\phi_{\nu\mathbf{k}}. \tag{3.10}$$

The basic approximations of the method lie in the calculation of the matrix elements of U:

$$<\nu\mathbf{k}|U|\nu'\mathbf{k}'>=\int\frac{d\mathbf{r}}{\Omega}e^{i(\mathbf{k}-\mathbf{k}')\cdot\mathbf{r}}u^*_{\nu 0}(\mathbf{r})U(\mathbf{r})u_{\nu' 0}(\mathbf{r}). \tag{3.11}$$

If $U(\mathbf{r})$ and $e^{i(\mathbf{k}-\mathbf{k}')\cdot\mathbf{r}}$ are nearly constant over a unit cell we have

$$< \nu\mathbf{k}|U|\nu'\mathbf{k}' > \simeq \delta_{\nu\nu'} \int \frac{d\mathbf{r}}{\Omega} U(\mathbf{r}) e^{i(\mathbf{k}-\mathbf{k}')\cdot\mathbf{r}} = \delta_{\nu\nu'} U_{\mathbf{k}\mathbf{k}'}. \tag{3.12}$$

where we used (3.7). For the calculation of the matrix elements of H, note that, from the definition (3.6),

$$H|\nu 0 >= E_{\nu 0}|\nu 0 >, \tag{3.13}$$

$$|\nu\mathbf{k} >= e^{i\mathbf{k}\cdot\mathbf{r}}|\nu 0 >, \tag{3.14}$$

where $E_{\nu 0}$ is the ν-th band energy at $\mathbf{k} = 0$. Hence, if $H = -\frac{\hbar^2}{2m_0}\nabla^2 + V_c$ with V_c the crystalline potential, we have

$$\begin{aligned} H|\nu\mathbf{k} > &= \left[-\frac{\hbar^2}{2m_0}\nabla^2 + V_c\right] e^{i\mathbf{k}\cdot\mathbf{r}}|\nu 0 > \\ &= e^{i\mathbf{k}\cdot\mathbf{r}}\left[\frac{\hbar^2}{2m_0}\left(k^2 - 2i\mathbf{k}\cdot\boldsymbol{\nabla} - \nabla^2\right) + V_c\right]|\nu 0 > \\ &= e^{i\mathbf{k}\cdot\mathbf{r}}\left(H - \frac{i\hbar^2\mathbf{k}\cdot\boldsymbol{\nabla}}{m_0} + \frac{\hbar^2 k^2}{2m_0}\right)|\nu 0 > \\ &= \left(E_{\nu 0} + \frac{\hbar^2 k^2}{2m_0}\right)|\nu\mathbf{k} > + e^{i\mathbf{k}\cdot\mathbf{r}}\frac{\hbar\mathbf{k}}{m_0}\cdot(-i\hbar\boldsymbol{\nabla})|\nu 0 > . \end{aligned}$$

Taking the scalar product with $< \nu'\mathbf{k}'|$ we obtain

$$< \nu'\mathbf{k}'|H|\nu\mathbf{k} >= \left(E_{\nu 0} + \frac{\hbar^2 k^2}{2m_0}\right)\delta_{\nu\nu'}\delta_{\mathbf{k}\mathbf{k}'} + \frac{\hbar\mathbf{k}\cdot\mathbf{P}_{\nu\nu'}}{m_0}\delta_{\mathbf{k}\mathbf{k}'} \tag{3.15}$$

with

$$\mathbf{P}_{\nu\nu'} = -i\hbar\int u^*_{\nu 0}\boldsymbol{\nabla}u_{\nu' 0}d\mathbf{r} \tag{3.16}$$

the momentum matrix elements which are responsible for the coupling between the different bands. Defining

$$H_{\nu\nu'}(\mathbf{k}) = \begin{cases} E_{\nu 0} + \dfrac{\hbar^2 k^2}{2m_0} & \nu = \nu' \\ \dfrac{\hbar\mathbf{P}_{\nu\nu'}\cdot\mathbf{k}}{m_0} & \nu \neq \nu' \end{cases} \tag{3.17}$$

we have

$$\sum_{\nu'} H_{\nu\nu'}(\mathbf{k})\phi_{\nu'\mathbf{k}} + \sum_{\mathbf{k}'} U_{\mathbf{k}\mathbf{k}'}\phi_{\nu\mathbf{k}'} = \varepsilon\phi_{\nu\mathbf{k}} \tag{3.18}$$

Finally, we go back to the $\mathbf{r}$ representation by multiplying to the left by $\frac{1}{\sqrt{\Omega}}e^{-i\mathbf{k}\cdot\mathbf{r}}$ and integrating over $\mathbf{k}$. Noting that

$$\frac{1}{\Omega}\int e^{-i\mathbf{k}'\cdot\mathbf{r}}H(-i\nabla)e^{i\mathbf{k}\cdot\mathbf{r}}d\mathbf{r} = H_{\nu\nu'}(\mathbf{k})\delta_{\mathbf{k}\mathbf{k}'} \tag{3.19}$$

we obtain the *multiband effective mass* equation:

$$\sum_{\nu'} H_{\nu\nu'}(-i\nabla)\psi_{\nu'}(\mathbf{r}) + U(\mathbf{r})\psi_{\nu}(\mathbf{r}) = \varepsilon\psi_{\nu}(\mathbf{r}) \tag{3.20}$$

where

$$\psi_{\nu}(\mathbf{r}) = \frac{1}{\sqrt{\Omega}}\int \phi_{\nu\mathbf{k}}e^{-i\mathbf{k}\cdot\mathbf{r}} \tag{3.21}$$

is the Fourier transform of $\phi_{\nu\mathbf{k}}$. The ψ_{ν}'s are called *envelope functions* since they contain only the long wavelength variations of the wavefunction. This is evident by making explicit the relationship between ψ_0 and the ψ_{ν}'s; from (3.9), (3.6) and (3.21) we have

$$\begin{aligned}\psi_0(\mathbf{r}) &= \sum_{\nu\mathbf{k}} \phi_{\nu\mathbf{k}}\frac{e^{i\mathbf{k}\cdot\mathbf{r}}}{\sqrt{\Omega}}u_{\nu 0}(\mathbf{r}) \\ &= \sum_{\nu} u_{\nu 0}(\mathbf{r})\psi_{\nu}(\mathbf{r}).\end{aligned}$$

We have reduced the problem of finding the rapidly varying ψ_0 to the problem of determining a set of slowly varying functions ψ_{ν}. Of course the accuracy of the method depends on the number of edges we put in the basis.

A final remark is necessary when eqs. (3.20) are applied to heterostructures. In fact the appropriate boundary conditions for the Φ_{ν} are complicated by the fact that the effective masses in (3.22) are functions of z since they depend on the material [23]. Moreover, since the $u_{\nu 0}(\mathbf{r})$'s are also different in different materials, in principle matching conditions on the $u_{\nu 0}(\mathbf{r})$'s should be used. Nevertheless, it is generally a good approximation to take the same functions in the different layers.

3.3 The Luttinger hamiltonian

Instead of using an high number of bands and calculate explicitly the quantities $\mathbf{P}_{\nu\nu'}$, the matrix elements $H_{\nu\nu'}(\mathbf{k})$ are often written as second-order polynomials whose coefficients have to be determined by fitting the bulk band structure of the material. Luttinger [24] proposed a widely used 6×6 hamiltonian which takes into account the heavy and light hole bands and the split-off band shown in fig. 3.2. Each of them is doubly degenerate due to the inversion symmetry of the crystal (Actually GaAs has no centre of symmetry but the the spin-orbit splitting due to this is negligibly small on the scale of energies we are interested in). The Kramer degeneracy is broken only in a non-symmetric potential $U(\mathbf{r})$ which, according to our initial statement of §3.1, we do not consider here. Since we are interested in an energy range of few tenths of meV below the valence band edge, we report here only the 4×4 Luttinger hamiltonian relative to the $J = 3/2$ states (heavy and light holes) and we neglect the influence of the split-off band. This approximation will be sufficient to deduce the basic features of the valence band in a confined structure. We label the four basis functions with $|3/2, J_z>$, with $J_z = 3/2, -3/2, 1/2, -1/2$. Then the Luttinger hamiltonian reads

$$H_L(\mathbf{k}) = \begin{pmatrix} H_{hh} & 0 & M & N \\ 0 & H_{hh} & N^* & -M^* \\ M^* & N & H_{lh} & 0 \\ N^* & -M & 0 & H_{lh} \end{pmatrix} \begin{matrix} |3/2,3/2> \\ |3/2,-3/2> \\ |3/2,1/2> \\ |3/2,-1/2> \end{matrix} \tag{3.22}$$

where

$$\begin{aligned} H_{hh} &= -\frac{\hbar^2}{2m_0}\left[(\gamma_1+\gamma_2)(k_x^2+k_y^2)+(\gamma_1-2\gamma_2)k_z^2\right] \\ H_{lh} &= -\frac{\hbar^2}{2m_0}\left[(\gamma_1-\gamma_2)(k_x^2+k_y^2)+(\gamma_1+2\gamma_2)k_z^2\right] \\ M &= \frac{\hbar^2}{2m_0}\left[2\sqrt{3}\gamma_3 k_z(k_x+ik_y)\right] \\ N &= \frac{\hbar^2}{2m_0}\left[\sqrt{3}\gamma_2(k_y^2-k_x^2)+i2\sqrt{3}\gamma_3 k_x k_y\right] \end{aligned}$$

Writing the matrix elements of (3.22) we have taken $E_{\nu 0} = 0$. The parameters γ_i are called Luttinger parameters. Their values are taken to fit experimental bulk band structure data and are available for the most common semiconductors.

Now we put eq. (3.22) in (3.20) with U a square potential to simulate the quantum well profile (bottom of fig. 3.1). For $k_x = k_y = 0$ the matrix (3.22) is diagonal and the four multiband effective mass equations reduce to the two decoupled equations

$$\left[\frac{\hbar^2(\gamma_1 - 2\gamma_2)}{2m_0}\frac{\partial^2}{\partial z^2} + U\right]\psi_h = E_h\psi_h,$$

$$\left[\frac{\hbar^2(\gamma_1 + 2\gamma_2)}{2m_0}\frac{\partial^2}{\partial z^2} + U\right]\psi_l = E_l\psi_l.$$

They look like Schrödinger equations except for the signs since holes must be confined in a barrier, *i.e.* a region of higher potential with respect to the surroundings (see fig. 3.1). In the limit of infinite U the energies are the same as in eq. (3.2) with the appropriate masses:

$$E_{ln} = -\frac{n^2\hbar^2\pi^2}{2m_0 d^2}(\gamma_1 + 2\gamma_2)$$

$$E_{hn} = -\frac{n^2\hbar^2\pi^2}{2m_0 d^2}(\gamma_1 - 2\gamma_2).$$

Due to the lighter mass, the light holes confinement energies are greater then those of the heavy holes. Following a common notation, we will indicate HH_n and LH_n the heavy and light subbands respectively.

Now we consider the in-plane dispersion. Neglecting for the moment the off-diagonal terms, the HH_n and LH_n subbands are

$$E_{HH_n} = E_{ln} - \frac{\hbar^2}{2m_0}(\gamma_1 + \gamma_2)(k_x^2 + k_y^2) \tag{3.23}$$

$$E_{LH_n} = E_{hn} - \frac{\hbar^2}{2m_0}(\gamma_1 - \gamma_2)(k_x^2 + k_y^2). \tag{3.24}$$

Note that the names "heavy holes" and "light holes" relate to the dispersion curves in the k_z direction while the effective mass ratio is reversed in the $k_x k_y$ plane. Then the HH_n

and LH_n subbands should cross somewhere. The off-diagonal terms couple the different heavy and light subbands together leading to anticrossing. If off-diagonal terms are to be taken into account numerical methods are necessary to solve the coupled differential equations. Several schemes have been devised so far to this aim. A typical calculation of the dispersion relations in a quantum well near the Fermi edge is shown in fig. 3.3 for a GaAs–$Al_xGa_{1-x}As$ quantum well structure at the Γ point. The band dispersion results

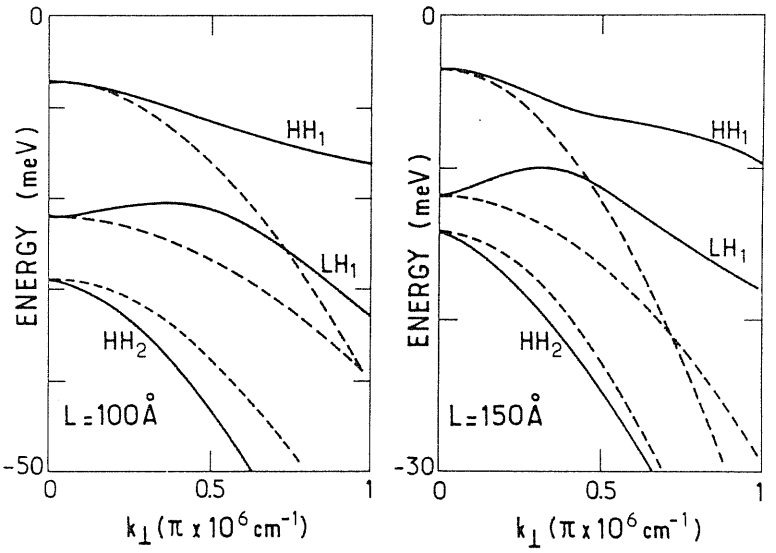

Figure 3.3: In-plane dispersion of the first valence subbands in a GaAs–$Al_xGa_{1-x}As$ quantum well from ref. [3]. Dashed lines are obtained neglecting off-diagonal terms in (3.22)

mainly from the coupling of the first three subbands, HH_1, HH_2 and LH_1. Anticrossing between HH_2 and LH_1 causes the positive sign of the LH_1 effective mass while the coupling between LH_1 and HH_1 is responsible for a strong non-parabolicity of HH_1. From fig. 3.3 it is also evident the anisotropy between the (1,0,0) and (1,1,0) directions of the Brillouin zone which leads to a warped shape of the Fermi surface.

3.4 A model for the valence band of confined systems

As we have seen, the exact calculation of the band structure in a confined system always involves the numerical solution of a set of coupled differential equations. In view of the semiclassical framework in which we will calculate the focusing spectrum of a two-dimensional hole gas (see chapter 2), we develop here a simple analytical model which gives the right dispersion of the topmost valence subband in the energy range we are interested in.

The results we have been reviewing so far suggest that, as far as symmetrical quantum wells are concerned where Kramer degeneracy occurs, a two band model, representing the HH_1 and HL_1 subbands, should be suitable to simulate the in-plane dispersion around Γ of the topmost valence subband in the confined system. In the spirit of the Luttinger hamiltonian, we can write an effective 2×2 hamiltonian whose elements are second order polynomials in $\mathbf{k}_\perp = (k_x, k_y)$ whose coefficients have to be determined by a fitting procedure. We write this hamiltonian as

$$H(\mathbf{k}_\perp) = \begin{pmatrix} H_h & S \\ S & H_l \end{pmatrix} \tag{3.25}$$

where

$$\begin{aligned} H_h &= \frac{\hbar^2 k_\perp^2}{2m_h} \\ H_l &= \Delta + \frac{\hbar^2 k_\perp^2}{2m_l} \\ S &= \alpha |k_x k_y| + \beta k_\perp^2 \end{aligned} \tag{3.26}$$

Neglecting the off-diagonal terms this hamiltonian gives two parabolic bands, with amplitude determined by m_h and m_l, which represent the HH_1 and LH_1 subbands, separated at $\mathbf{k}_\perp = 0$ by a gap Δ which simulates the different splitting of HH_1 with respect to LH_1. The HH_1 subband at $\mathbf{k}_\perp = 0$ has been taken as the zero of energy. In this approximation the two subbands cross each other at finite $\mathbf{k}_\perp$. The off–diagonal term S introduces an

isotropic (α) and an anisotropic (β) coupling between the subbands. The isotropic term is responsible for non-parabolicity of the HH_1 subband due to anti-crossing. The anisotropic term then introduces a warping of the Fermi surface.

The coupling constants α and β and the effective masses m_h and m_l are determined fitting an exact calculation, carried out in the envelope function approximation following the scheme described in ref. [26], for a GaAs–$Al_xGa_{1-x}As$ quantum well 140Å wide. The parameters obtained are listed in tab. 3.1. In fig. 3.4(a) the result for the model hamilto-

m_h/m_0	m_l/m_0	α	β	Δ
0.165	0.743	$7.7eV\AA^2$	$5.0eV\AA^2$	$4.5meV$

Table 3.1: Values of the parameter used in eq. (3.25). m_0 is the electron rest mass.

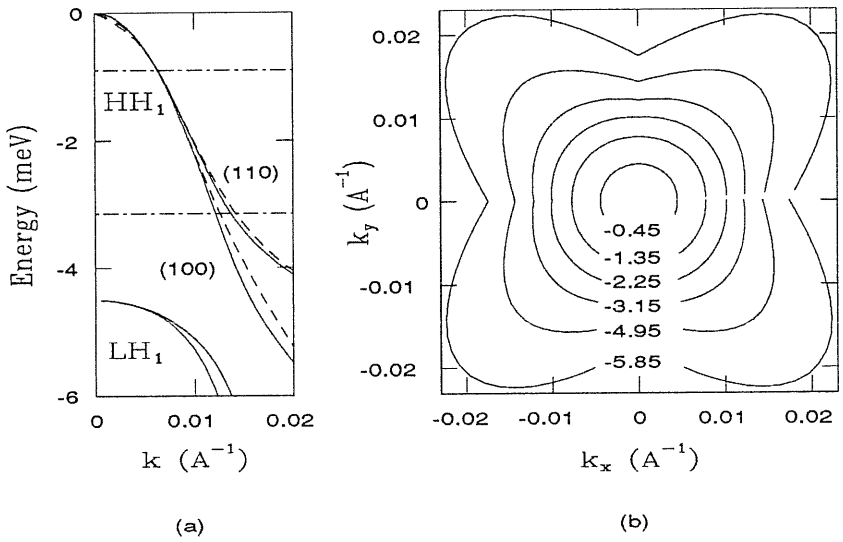

Figure 3.4: a) Valence band dispersion of a 140Å GaAs quantum well along the in-plane (100) and (110) directions. Dashed lines: exact calculation Full lines: model hamiltonian of eq. (3.25). Horizontal lines indicate the energies used in the calculation of the TEF spectra of fig. 4.3. b) Equal energy contours for the HH_1 subband according to our model. Energies are in meV.

nian (3.25) (solid lines) is compared with the exact calculation (dashed line) for the HH_1 subband. Note that with our two band model only the highest HH_1 subband dispersion can be reproduced. This is because we loose the coupling with the HH_2 subband, whose

effect is explained in the previous paragraph, which is not present in our model. To obtain the right HH_1 dispersion, we must take an unphysical value of Δ, much smaller then the real gap HH_1–LH_1. For the same reason our model does not reproduce the positive effective mass of LH_1.

In fig. 3.4(b) equal energy contours are reported at various energies lying between the two subbands. Note that near the edge, except for the sign of the mass, the situation is much similar to the conduction band, the HH_1 band is parabolic and equal energy contours are isotropic, while, at lower energies, both non-parabolicity and warping of the Fermi surface are present.

Our model is intended to simulate the in-plane dispersion in a quantum well. This means that the effects of the asymmetry of the confining potential is neglected. These effects amount in the splitting of the doubly degenerate levels at finite $\mathbf{k}_\perp$ in systems where spin-orbit coupling is present if no centre of inversion exists. This splitting is particularly high in the valence band due to the highest spin-orbit coupling [25].

Chapter 4

Focusing of a two-dimensional hole gas

In this chapter we use the two-band model conceived in §3.4 to determine the edge states and the focusing spectrum for a two-dimensional hole gas by following the same steps which led to the electronic edge states. We analyse the results and interpret them in terms of the effects of warping of the Fermi surface and non-parabolicity of the valence band.

4.1 Edge magnetic states of the two-dimensional hole gas

In §2.1 we have seen that the quantum states of a charge in a magnetic field in proximity of a boundary, namely the edge magnetic states, can be determined in a semiclassical approximation by means of a simple geometric condition on the area of the orbits. Here we determine the edge magnetic states resulting from our model hamiltonian (3.25).

Diagonalization of eq. (3.25) gives a secular equation from which the equal energy contours can be determined. We use for the moment eq. (3.25) with $\beta = 0$. Then, from the condition $det(H - I\varepsilon) = 0$, where H is defined by eq. (3.25) and I is the 2×2 identity

matrix, we have that the equal energy contour at energy ε is given by the polar curve

$$k^2(\theta) = \frac{\Delta m_l}{\hbar^2} \frac{-[1+\bar{\varepsilon}+\bar{\varepsilon}/\eta] + [(1+\bar{\varepsilon}-\bar{\varepsilon}/\eta)^2 + \bar{\varepsilon}(\bar{\varepsilon}+1)\bar{\alpha}^2 \sin^2 2\theta]^{1/2}}{1 - \frac{\bar{\alpha}^2\eta}{4}\sin^2 2\theta} \tag{4.1}$$

for the higher HH_1 subband, where θ is the polar angle (see fig. 4.1) and we used the adimensional quantities

$$\bar{\alpha} = \frac{\alpha}{\hbar^2/2m_h}, \qquad \bar{\varepsilon} = \frac{\varepsilon}{\Delta}, \qquad \eta = \frac{m_l}{m_h}. \tag{4.2}$$

Note that (4.1) reduces to (2.15) in the no-coupling limit $\bar{\alpha} = 0$. Now we scale it by l_m^4 to

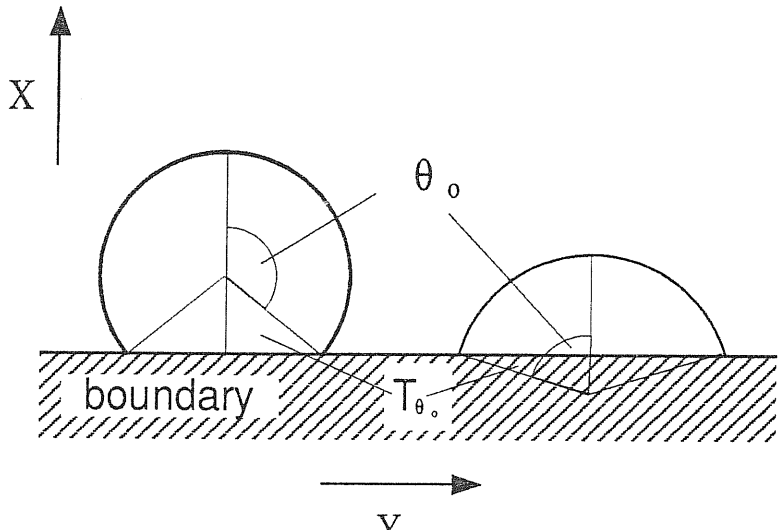

Figure 4.1: Geometrical definitions of the quantities θ_0 and T_{θ_o}. The left panel represent an orbit with the centre outside the barrier (negative k_y). The right panel represents an orbit with the centre inside the barrier (positive k_y).

get the real space orbits. Then the flux enclosed by the semiclassical orbit is

$$\Phi = \int_S \mathbf{B} \cdot d\boldsymbol{\sigma} = 2l_m^4 B \int_0^{\theta_0} k^2(\theta) d\theta - 2T_{\theta_o} \tag{4.3}$$

where θ_0, defined in fig. 4.1, can be connected geometrically to k_y by the identity

$$k(\theta_0)\cos\theta_0 = -k_y \tag{4.4}$$

and $T_{\theta_o} = l_m^4 k^2(\theta_0) \sin 2\theta_0$ is the area of the triangular sector in fig. 4.1. Putting everything together we have

$$\begin{aligned}\Phi &= l_m^4 \frac{\Delta m_l}{\hbar^2} \left\{ -[1+\overline{\varepsilon}+\overline{\varepsilon}/\eta] \int_0^{2\theta_0} \frac{d\theta}{1-\kappa \sin^2 2\theta} \right. \\ &\left. +|1+\overline{\varepsilon}-\overline{\varepsilon}/\eta| \int_0^{2\theta_0} \frac{1-q\sin^2 2\theta}{1-\kappa \sin^2 2\theta} \right\} d\theta - 2T_{\theta_o} \end{aligned} \tag{4.5}$$

where we denoted

$$\kappa = \frac{\overline{\alpha}^2 \eta}{4}, \qquad q = -\overline{\varepsilon}(\overline{\varepsilon}+1) \left[\frac{\overline{\alpha}}{1+\overline{\varepsilon}-\overline{\varepsilon}/\eta} \right]^2 . \tag{4.6}$$

The first integral can be evaluated directly to give

$$(1-\kappa)^{-1/2} \arctan t(1-\kappa)^{1/2} \Big|_{t=\tan 2\theta_0} \tag{4.7}$$

while after some manipulation the second integral gives

$$(1-q/\kappa)\Pi(2\theta_0, \kappa, q) + (q/\kappa) F(2\theta_0, q) \tag{4.8}$$

being $F(\varphi, q)$ and $\Pi(\varphi, \nu, t)$ the elliptic integrals of the first and third kind respectively. Finally, the Bohr–Sommerfeld quantization condition for the hamiltonian (3.25) with $\beta = 0$ reads

$$\begin{aligned} l_m^2 \frac{\eta \Delta}{\hbar \omega_c^h} \left\{ -[1+\overline{\varepsilon}+\overline{\varepsilon}/\eta] (1-\kappa)^{-1/2} \arctan t(1-\kappa)^{1/2} \Big|_{t=\tan 2\theta_0} + [1+\overline{\varepsilon}-\overline{\varepsilon}/\eta] \cdot \right. \\ \left. \cdot (1-q/\kappa)\Pi(2\theta_0, \kappa, q) + (q/\kappa) F(2\theta_0, q) \right\} - 2k^2(\theta_0) \sin 2\theta_0 = 2\pi(n-\gamma) \end{aligned} \tag{4.9}$$

where $\omega_c^h = m_h c/eB$.

Even if the approximation $\beta = 0$ allows an analytical determination of the quantization condition, it has the drawback that the two bands intersect along the $k_x = 0$ and $k_y = 0$ directions, where the off-diagonal term S vanish, which is an unphysical result. The equal

energy contour for non-vanishing β has a slightly more complicated form than eq. (4.1):

$$k^2(\theta) = \frac{\Delta m_l}{\hbar^2} \frac{-[1+\overline{\varepsilon}+\overline{\varepsilon}/\eta] + [(1+\overline{\varepsilon}-\overline{\varepsilon}/\eta)^2 + 4\overline{\varepsilon}(\overline{\varepsilon}+1)(\frac{\overline{\alpha}}{2}|\sin 2\theta| + \overline{\beta})^2]^{1/2}}{1-\eta(\frac{\overline{\alpha}}{2}|\sin 2\theta| + \overline{\beta})^2} \tag{4.10}$$

where we used the adimensional quantity $\overline{\beta} = \beta/(\frac{\hbar^2}{2m_h})$. Then a numerical integration has been used to calculate the area enclosed by this curve and find the energy bands, and the results tested with those obtained from eq. (4.9) in the $\beta = 0$ approximation.

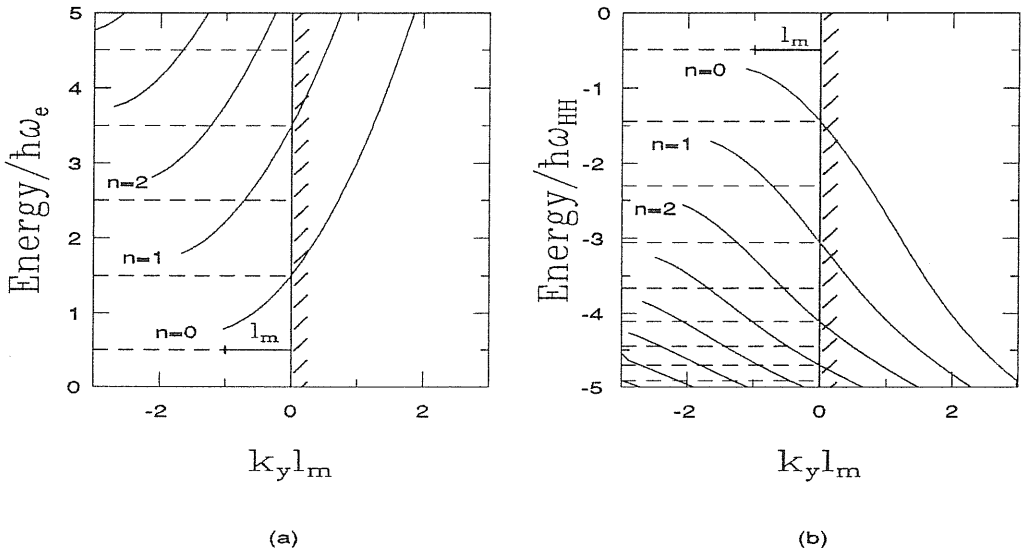

Figure 4.2: Magnetic edge states for parabolic dispersion (a) and for the HH subband (b) calculated at $B = 1.2T$ corresponding to $l_m = 2.3 \times 10^{-8}m$. Energies are in units of the cyclotron frequency. The cyclotron frequency at $1.2T$ for GaAs conduction electrons is $\hbar\omega_c = 2.1meV$ corresponding to $m^\star = 0.067m_0$ and for the HH subband is $\hbar\omega_{HH} = 0.84meV$ corresponding to $m^\star = 0.165m_0$ where $m^\star$ is the effective mass and m_0 the electron rest mass. The shaded area indicates the position of the infinite barrier. Dashed horizontal lines indicate the non dispersive bulk Landau levels.

The valence electrons edge energies resulting from our model (3.25) are shown in fig. 4.2(b), while in 4.2(a) the conduction electrons diagram of fig. 2.2 is repeated for comparison. Some differences are recognized; while the parabolic dispersion of conduction electrons results in equidistant bulk[1] Landau levels, bulk valence states get closer going

[1] In this context, bulk states are the 2D Landau levels as opposed to surface or edge states close to the barrier.

to lower energies because, due to the non–parabolic behaviour of the HH subband, the effective mass (and consequently the cyclotron frequency ω_c) is not well defined anymore. The energy dispersion is therefore similar in the two cases for energies near to the HH_1 edge, but is modified at lower energies. Note that, due to the anisotropy of the Fermi surface, different crystallographic directions of the boundary are not equivalent. Fig. 4.2(b) is obtained for a boundary in the $(1,0,0)$ direction.

4.2 Coherent focusing in a two-dimensional hole gas

We are now in the position to calculate focusing spectra for a two-dimensional hole gas from eq. (2.18). We must choose a Fermi energy, determine at each field the allowed n_{max} edge states at that energy, as explained in chapter 2, and put them in eq. (2.18). Spectra calculated from (2.18) with different values of E_F are shown in fig. 4.3. Focusing spectra were obtained averaging for L over a range of $100nm$ around $3\mu m$ to simulate the combined width of the injector and the collector [7].

Fig. 4.3(a) shows the spectrum obtained at E_F near the band edge (higher dashed-dotted line in fig. 3.4), where orbits are isotropic, as shown in the corresponding inset, and the HH_1 subband is parabolic. For this reason the results are independent of the crystallographic direction of the barrier and are expected to resemble those obtained in [7] for conduction electrons. This is in fact the case; a fine structure appears superimposed onto the peaks at classical focusing fields B_{focus} due to the interference between different magnetic edge states, with an amplitude which increases with the field, in agreement with the experimental results. At the highest fields the maxima in the current do not occur anymore at multiples of B_{focus} even if at this energy the cyclotron frequency is still well defined (see previous paragraph).

The above results can be explained as follows. We have already noted in chapter 2 that the number n_{max} of modes k_n at E_F is equal to the number of occupied Landau levels at the same energy. At low field, where Landau levels are dense in energy, many k_n are

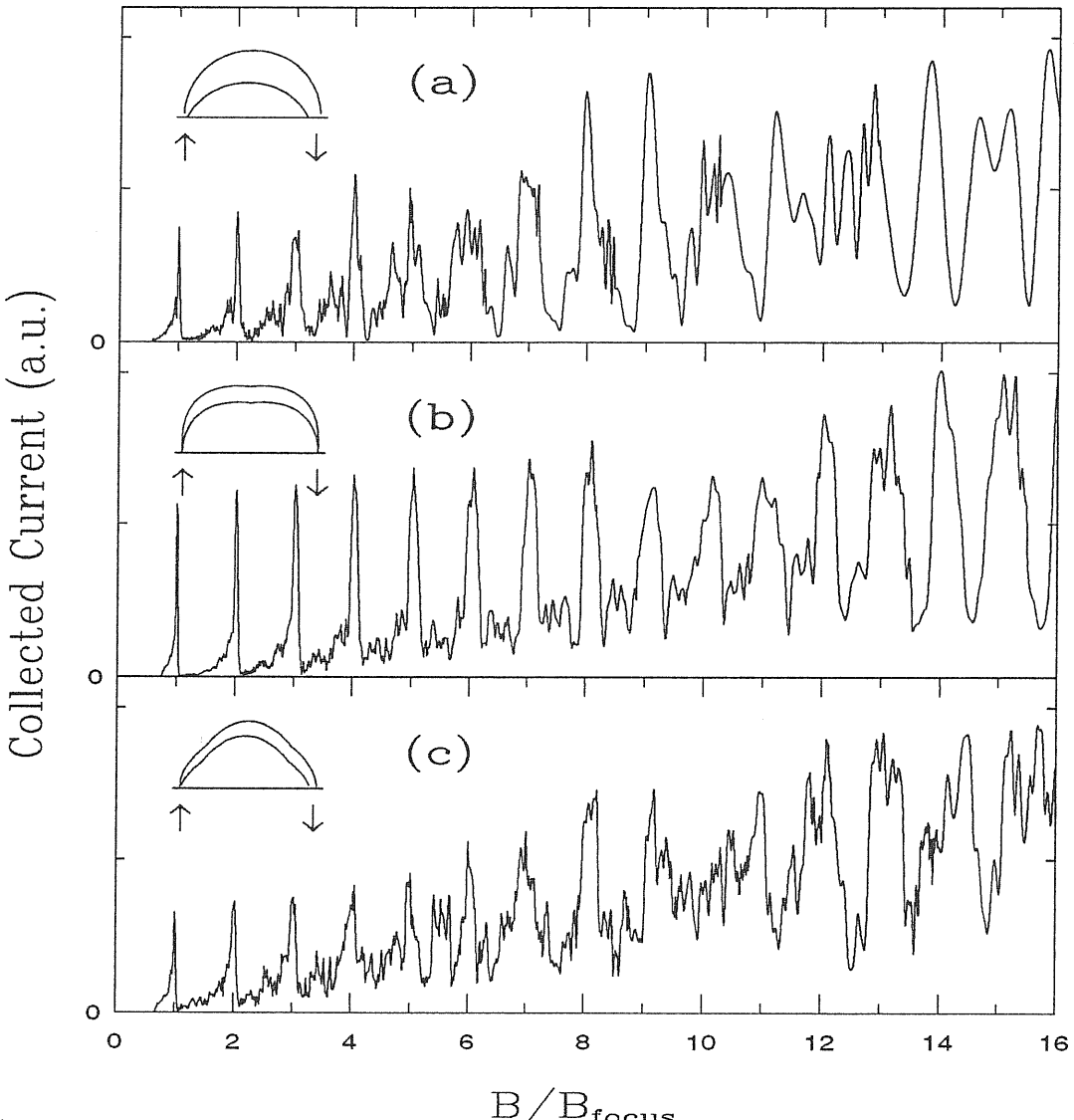

Figure 4.3: Calculated TEF spectra at different E_F's with different orientations of the barrier. a) $E_F = -0.9meV$; b) $E_F = -3.15meV$ with the barrier along the (100) direction; c) $E_F = -3.15meV$ with the barrier along the (100) direction. The resulting focusing fields are: a) $B_{focus} = 0.027T$, b) $B_{focus} = 0.054T$ and c) $B_{focus} = 0.059T$. The insets show the shape of the relative quasi–classical orbits.

allowed at E_F with positive and negative values. On average, therefore, the different terms in eq. (2.18) cancel each other, except those around $n_{max}/2$ or $k_n \sim 0$. In metals, due to the small λ_F, a very high number of k_n is occupied even at high fields so that the only contribution to the current is obtained from constructive interference at B_{focus} of states with $k_n \sim 0$, which correspond to the classical skipping orbits centered on the boundary. In semiconductors, on the contrary, due to the higher λ_F, few states are allowed at E_F so that superposition of waves may lead to fluctuations in the current even at low field where, in fact, the fine structure appear in spectra. With increasing field, the separation between Landau levels increases as well and n_{max} decreases. Due to the small number of contributing states, the interference manifests itself with large oscillations in the collected current. These results confirm that the fine structure and the strong oscillations with non-monotonic intensity observed in experimental spectra are the effect of the coherent nature of electron focusing in semiconductors and they clarify the role played by the edge magnetic states.

Fig. 4.4 shows the influence of the dimensions of the quantum point contacts. Spectra have been calculated at the same energy of fig. 4.3(a) with a simulated width W of $100nm$ (top) and of $400nm$ (bottom) of the collector. In agreement with the experimental results [10], the spectrum relative to the larger collector has broader peaks with monotonously increasing intensity, while the fine structure is strongly reduced. The structure of the peaks therefore compares to that of spectra taken in metals. Note that at $B > 0.2T$ the focusing peaks disappear completely since the cyclotron radius become smaller of the collector width and the resolution for the focusing is lost.

Our calculated TEF spectra are strongly modified at lower energy if the barrier is taken along the (100) direction as shown in fig. 4.3(b): peaks at the classical focusing fields are sharper and B_{focus} remains well defined in a wider range of fields so that the spectrum is more similar to the classical case observed in metals. Since we are still in a quantum regime, the reason for this behaviour must be sought in the shape of the quasi–classical

orbits. In fact, as shown in the insets of figs. 4.3(a) and 4.3(b), two orbits corresponding to different k_n leaving a point–like injector, reach the collector in a narrower spatial range in the case of warped orbits (fig. 4.3(b)) with respect to the case of the isotropic ones (fig. 4.3(a)). This effect is completely due to the warped shape of the Fermi surface, *i.e.* the crystalline potential helps the magnetic field to keep the electrons focused onto the collector.

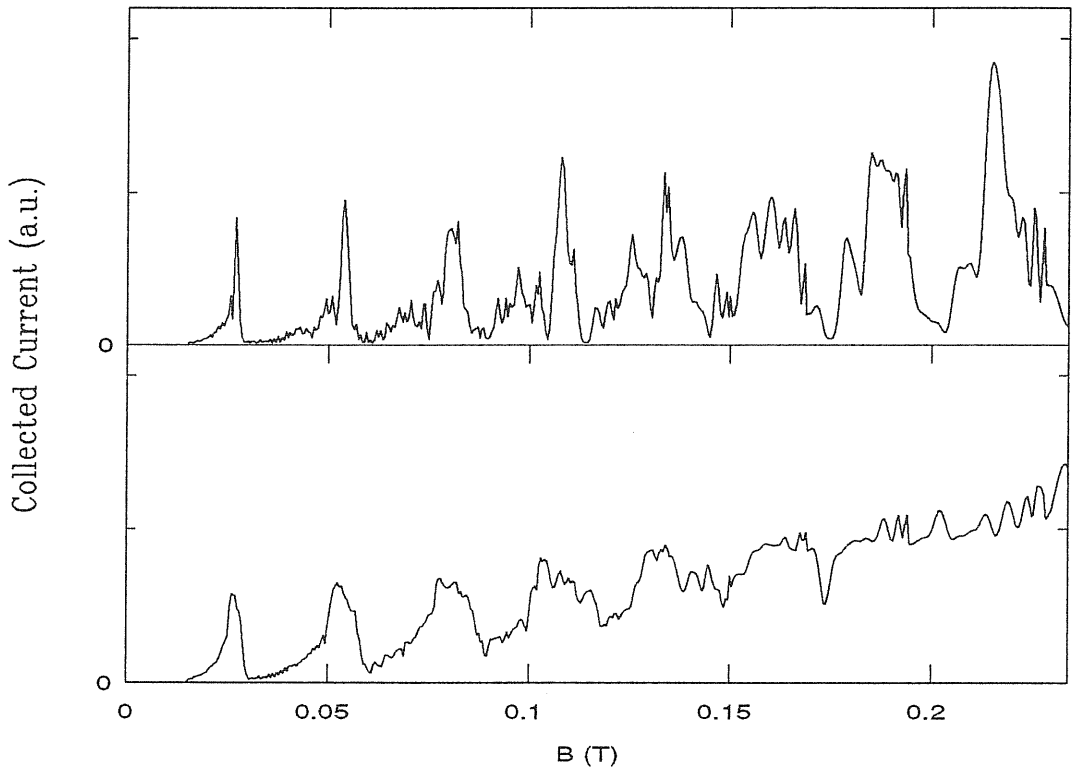

Figure 4.4: Focusing spectra calculated at the same energy of fig. 4.3(a) with two different widths W of the collector. Top: $W = 100nm$. Bottom: $W = 400nm$. The focusing field is $0.027T$.

The situation modifies again if the barrier is placed along the (110) crystallographic direction as shown in fig. 4.3(c). The resulting spectrum, obtained at the same Fermi energy as fig. 4.3(b), displays again the fine structure because different orbits are not focused anymore onto the collector by the crystal, as shown in the inset.

The non–parabolicity of the valence band shows up also in the behaviour of the focusing

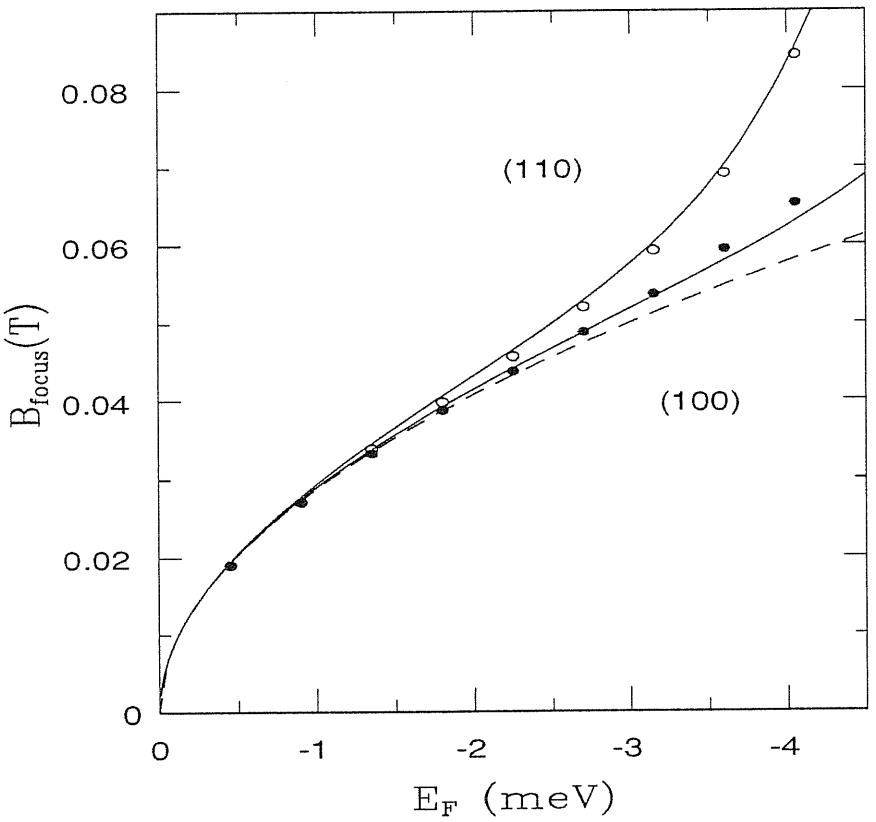

Figure 4.5: Focusing fields vs. E_F obtained from calculated TEF spectra with the barrier along the (100) direction (solid points) and the (110) direction (open points). Full lines indicate the focusing field calculated from $B_{focus} = 2\hbar k(E_F)/eL$ in the two directions from the function $k(\varepsilon)$ resulting from eq. (3.25). Dashed line indicates the same calculation for a parabolic dispersion with $m^\star = 0.165 m_0$.

field as a function of the Fermi energy as shown in fig. 4.5. The focusing fields, calculated for several E_F's and for barriers along the (100) and (110) directions, deviate from the square root behaviour ensuing from a parabolic dispersion (see eq. (1.5)). Once we plot the HH subband along the two (100) and (110) directions by scaling $k(\varepsilon)$ according to (1.5), it can clearly be seen that the calculated values of B_{focus} fall onto the dispersion in analogy to the electronic case. It should be noted that only the dispersion in the direction of the barrier contribute to define B_{focus} so that, at least in principle, TEF experiments in a 2D hole gas could probe directly the band structure.

To summarize, we found that the details of the band structure strongly affect the

calculated TEF spectra. In particular the anisotropy of the valence band influences both the intensity of the fine structure and the periodicity of the TEF spectra. We believe that these effects should be observable since the use of the semiclassical approach is appropriate in the low magnetic field regime of our calculations, where an high number of edge states is occupied.

Bibliography

[1] H. van Houten, B. J. van Wees, J. E. Mooij, C. W. J. Beenakker, J. G. Williamson and C. T. Foxon, Europhys. Lett. **5**, 721 (1988).

[2] T. Ando, A. B. Fowler and F. Stern, Rev. Mod. Phys. **54**, 437 (1982).

[3] G. Bastard, *Wave mechanics applied to semiconductor heterostructures*, Les éditions des physique.

[4] C. Weisbuch in *Semiconductros and Semimetals*, Vol. 24, Academic Press.

[5] Yu. V. Sharvin and L. M. Fisher,JETP Lett. **1**, 152 (1965).

[6] V. S. Tsoi, JETP Lett. **19**, 70 (1974).

[7] C. W. J. Beenakker, H. van Houten and B. J. van Wees, Europhys. Lett. **7**, 359 (1988).

[8] G. Timp, A. M. Chang, P. Mankiewich, R. Behringer, J. E. Cunningham, T. Y. Chang and R. E. Howard, Phys. Rev. Lett. **59**, 732 (1987).

[9] G. Goldoni and A. Fasolino, in press

[10] H. van Houten, C. W. J. Beenakker, J. G. Williamson, M. E. I. Broekaart, P. H. M. van Loosdrecht, B. J. van Wees, J. E. Mooij, C. T. Foxon and J. J. Harris Phys. Rev. B **39**, 8556 (1989).

[11] Yu. V. Sharvin, Sov. Phys. – JETP **21**, 655 (1965).

[12] Yu. V. Sharvin and N. I. Bogatina,Sov. Phys. – JETP **29**, 419 (1969).

[13] V. S. Tsoi, Sov. Phys. – JETP **41**, 927 (1975).

[14] P. A. M. Benistant, G. F. van de Valle, H. van Kempen and P.Wyder, Phys. Rev. B **33**, 690 (1986).

[15] P. C. van Son, H. van Kempen and P. Wyder, Phys. Rev. Lett. **58**, 1567 (1987).

[16] D. A. Wharam, T. J. Thornton, R. Newbury, M. Pepper, H. Ahmed, J. E. F. Frost, D. G. Hasko, D. C. Peacock, D. A. Ritchie and G. A. C. Jones, J. Phys. C **21**, L209 (1988).

[17] L. D. Landau and E. M. Lifshitz, *The classical theory of fields*, Pergamon Press, Oxford.

[18] A. H. MacDonald and P. Středa, Phys. Rev. B **29**, 1616 (1984).

[19] C. Kittel, *Quantum theory of solids*, John Wiley & Sons.

[20] See *e.g.* L. D. Landau and E. M. Lifshitz, *Quantum mechanics (Non-relativistic theory)*, Pergamon Press, Oxford.

[21] L. S. Schulman, *Tecniques and applications of path integration*, Wiley, New York.

[22] See *e.g.* F. Bassani and G. Pastori Parravicini, *Electronic states and optical transitions in solids*, Pergamon Press, Oxford, 1975

[23] D. J. Ben-Daniel and C. B. Duke, Phys. Rev. **152**, 683 (1966)

[24] J. M. Luttinger and W. Kohn, Phys. Rev. **97**, 869 (1955); J. M. Luttinger, Phys. Rev. **102**, 1030 (1956).

[25] D. A. Broido and L. J. Sham,Phys. Rev. B **31**, 888 (1985).

[26] M. Altarelli, U. Ekenberg and A. Fasolino Phys. Rev. B **32**, 5138 (1985).